Cloud Motion Identification Algorithms Based on All-Sky Images to Support Solar Irradiance Forecast

Lydie Magnone, Fabrizio Sossan, Enrica Scolari, Mario Paolone

Cloud Motion Identification Algorithms Based on All-Sky Images to Support Solar Irradiance Forecast

Lydie Magnone, Fabrizio Sossan, Enrica Scolari, Mario Paolone
École Polytechnique Fédérale de Lausanne, Switzerland

***Abstract*—Cloud motion is a cause of direct irradiance variations at ground level and determines significant fluctuations of PV generation. In this work, we investigate on how integrating information on clouds motion extracted from all-sky images into a time series-based forecasting tool for global horizontal irradiance (GHI) to enhance its prediction performance. We consider three different cloud motion algorithms: heuristic motion detection (HMD), particle image velocimetry (PIV), and a persistent model. The HMD method is originally proposed in this paper. It consists in choosing the cloud motion vector leading to the best cloud map prediction considering the most recent sky images. Results show that integrating the information of the predicted cloud coverage in the circumsolar area leads to a decrease of the width of the GHI prediction intervals up to 2% for prediction horizons in the range 1 to 10 minutes.**

I. Introduction

The trend towards decentralized control and short-term redispatch of conventional generation in power systems has increased the focus on short-term forecasting of stochastic generation at low aggregation level. Examples are in the field of control of microgrids, active distribution networks, and photovoltaic (PV) self-consumption, where the availability of predictions for specific PV installations is required, e.g. [1]. Whereas traditional satellite-based forecasting methods fail to meet spatial and temporal resolution requirements, recent developments in the existing literature have proposed the application of time series based methods to learn patterns of PV production/irradiance from historical observations, see [2]. With respect to the sole use of historical irradiance observations, the integration of information from all-sky images (ASIs) establishes a step further in terms of available knowledge thanks to enabling the identification of clouds position and motion.

The tool-chain to infer irradiance predictions from ASIs generally consists in the following main steps: *i)*, image preprocessing, *ii)*, cloud detection (i.e. deciding whether each pixel of the image correspond to a cloudy or clear sky point), *iii)*, cloud motion identification, and, *iv)*, elaboration of irradiance predictions. In this work, cloud detection is performed by applying Schmidt's algorithm [3].

First, we focus on the performance analysis of cloud motion algorithms. We propose an original method, called heuristic motion detection (HMD), and we compare its performance against those of particle image velocimetry (PIV, from the existing literature) and a persistent benchmark method. Performance is evaluated in terms of misclassification which is achieved when predicting the future position of clouds (so-called cloud map). In order to exclude from the performance assessment the errors due to wrong segmentation, we consider a set of manually segmented images (where the assignment cloud/clear sky pixel is performed by human visual inspection) as a ground truth value.

Second, the predicted cloud map is used to compute the amount of cloudy pixels in a circumsolar area. This information is used as an additional influential variable in a time series based forecasting tool for prediction intervals (PIs) of the global horizontal irradiance (GHI) considering 1, 2, 5 and 10 minutes forecast horizons.

This paper is organized as follows: Section II describes the state-of-the-art, Section III presents the methods, Section IV is for results, and Section V states the conclusions.

II. State-of-the-art

The first work focusing on intra-hour irradiance forecast considering information from sky-images is described by Chow et al. in [4]. Cloud shadows projected on the ground are estimated using two-dimensional cloud maps generated from the cloud cover. Cloud motion vectors are generated by processing two consecutive sky images. Marquez and Coimbra, [5], predict the direct normal irradiance (DNI) by considering the clouds in the vicinity of the sun and detect cloud motion with PIV. Their irradiance forecasts outperform the persistence model for forecast horizons in the range 3 to 15 min, with the most accurate forecasts at 5 min. Chen et al. in [6] apply PIV to compute a velocity vector per cloud and develop a multi-scale cloud block matching strategy to account for clouds deformations. Another technique for cloud tracking is *optical flow*, which consists of a collection of apparent velocities of objects in an image. It is applied to cloud motion detection for predicting sun occlusions in [7], using consecutive frames shot at a few seconds distance. Since in this works we consider frames at 1 minute resolution, optical flow is not considered. Quesada-Ruiz et al. in [8] propose a method for cloud tracking applied to intra-hour DNI forecast. A sector-based method is used to detect the direction of motion of potentially sun-blocking clouds, and an adjustable-ladder method focuses on sky regions that potentially affects DNI values. Finally, Bernecker et al. in [9] introduce non-rigid registration for detecting cloud motion.

This research received funding from the Swiss Competence Center for Energy Research (FURIES) and by the SNSF NRP70 "Energy Turnaround".

A sun occlusion probability is filtered by a Kalman filter to obtain continuous GHI forecasts for up to 10 min.

Several works focus on the inclusion of all-sky images features into machine learning methods. In [8], a DNI forecasting model is developed based on an artificial neural network (ANN). It uses cloud cover time series (estimated from ASIs) in combination with DNI historical observations to forecast DNI on the 5 and 10 minutes look-ahead time. A hybrid model to construct DNI prediction intervals is proposed in [10]. It exploits information from ASIs, which are integrated to a support vector machine and ANNs. Authors of [11] propose a model for intra-hour GHI forecasting based on the k-nearest-neighbors (kNN). It exploits local observations and information from ASIs and delivers point predictions and PIs of both GHI and DNI. The inclusion of ASIs improves the definition of the PIs. Authors of [12] incorporate measured irradiance data with features extracted from ASIs to deliver point predictions, achieving to foresee irradiance variations accurately.

III. Methods

The tool-chain used to compute GHI prediction intervals is shown in Fig. 1 and consists in the following steps (detailed in the rest of this section):

1) Image acquisition.
2) Image pre-processing. The horizon (i.e. topological features and nearby objects) is removed from the image, and the distortion due to the fish-eye lens is corrected with a geometrical transformation. Besides, the sun position is determined as a function of the sun zenith and azimuth values.
3) Cloud detection. Each pixel of the image is labeled as a cloud or clear sky. The result of the segmentation is a binary image called cloud map.
4) Cloud motion identification. It consists in estimating the cloud movement. We consider three methods: (i) HMD, a method proposed in this paper for the first time, (ii) PIV, and (iii) the persistence predictor. Each cloud motion algorithm returns one motion vector (a single one for the whole image), called *global motion vector*.
5) Cloud map forecasting: the cloud map is translated by applying the global motion vector. This leads to the forecasted cloud map.
6) Local cloud cover computation. Given the forecasted cloud map, it consists in computing the percentage of cloudy pixels in a specific area around the sun.
7) GHI prediction intervals computation. We extend a time series-based probabilistic prediction tool from our previous work [2], which was originally fed with GHI measurements only. We add the local cloud cover as an influential variable to explain GHI variations.

A. Image acquisition

Images are from an USB 2 megapixel camera with CMOS sensor and fish-eye lens. It is installed on the roof of our laboratory building, pointing at the zenith. Frames are taken at 1 minute resolution with manual exposure time to limit overexposure of the circumsolar area. The framegrabber is a Raspberry PI computer.

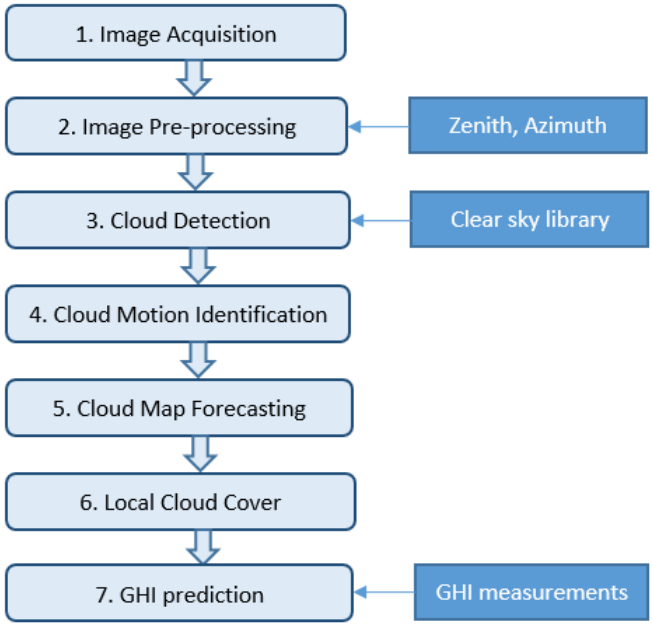

Fig. 1. Process of GHI forecast with all-sky images.

B. Image pre-processing

The sun position is determined by converting the solar zenith and azimuth coordinates (calculated by using the PV Performance Modeling Toolbox by Sandia National Laboratories [13]) into pixels coordinates. We use the Zenithal Equal Area Projection method from [14]. The image distortion is corrected by applying the procedure described in [15], which requires a series of pictures of a chessboard (shot offline). The sun coordinates are then transformed into undistorted coordinates. Finally, the horizon features (trees, buildings, mountain ridges) are removed by using a binary mask, manually determined offline.

C. Cloud detection

It consists in determining if a pixel corresponds to a cloudy or clear sky point. A common procedure for cloud detection consists in computing the red to blue ratio (RBR) of the image color channels, which generally achieves a good degree of separation between clouds (high RBR) and clear sky pixels (low RBR). However, misclassification occurs due to very bright clear sky pixels (high RBR) in the circumsolar area and very dark clouds (low RBR). Authors of [3] proposed an augmented RBR definition. It makes use of a clear sky library to achieve a better segmentation of the circumsolar pixels, and solar saturation and gray intensity level to account for dark clouds. The pixel RBR we use in this work is defined as:

$$R_{mod} = R_{orig} - R_{CSL}(a\,(2\,S - 1) - b\,(I - c)), \quad (1)$$

where R_{orig} is the RBR of the considered image, R_{CSL} is the corresponding RBR value on a clear sky picture (selected from a clear sky library such that the sun position is as close as possible to the target picture), S is the saturation and refers to the percentage of saturated pixels in a circumsolar region with radius r, I is the gray intensity level, while a, b and c are tuning parameters. Finally, a pixel is marked as a cloud if its modified RBR value in (1) is larger than a threshold R_{thresh} and vice-versa.

The free parameters a, b, c, r, R_{thresh} involved in the cloud detection procedure are determined in order to give the best performance with our imaging setup. They are chosen with the following heuristic procedure: 40 images referring to periods with different weather conditions and sun position are selected and manually segmented; therefore, the same images are automatically segmented by using different possible combinations of the parameters in the ranges shown in Table I. The best values of the parameters are chosen as those leading to the best cloud map estimation.

TABLE I
SEGMENTATION PARAMETER SETTING

Name	Selected value	Tested range
a	0.6	0.3 to 1, with a step of 0.1
b	0.001	0 to 0.003, with a step of 0.001
c	220	130 to 220, with a step of 10
R_{thresh}	0.2	0.1 to 1, with a step of 0.1
r (pixels)	30	30 to 60, with a step of 10

D. Cloud Motion Identification

In this section, we first describe the formulation of the proposed method for cloud motion identification, the HMD. Later, we summarize the ideas behind PIV and describe the persistence model. As mentioned earlier, we assume in this work that all the visible clouds move uniformly, i.e. with same direction and speed. Under this assumption, there is a unique motion vector, called *global motion vector*.

Let us consider a set of pictures taken at 1 minute resolution. The problem consists in producing a binary image which contains the 1, 2, 5, or 10 minutes ahead predictions of the clouds position.

1) Heuristic Motion Detection (HMD): The HMD procedure is the following:

- we consider two consecutive cloud maps at time t–1 (A) and t (B);
- n binary cloud maps $A_1, \ldots, A_n$ are generated by translating the cloudy map A according to a random motion vector $\mathbf{v} = (u, v)$ with $\mathbf{v} \in \mathbb{R}^2$. We denote by (i, j) the pixel location. Then, the future position of a binary pixel is:

$$[i(t), j(t)] = [i(t-1) + u, j(t-1) + v] \qquad (2)$$

  In this work we consider 400 random vectors $\mathbf{v}$.
- each cloud map $A_1, \ldots, A_n$ is compared against B in terms of matching error defined as the sum of the misclassified pixels, see Section IV-B.
- the motion vector that generates the lowest matching error is selected.

2) Particle Image Velocimetry (PIV): In brief, PIV consists in comparing two consecutive pictures by evaluating the cross-correlation between portions of the images, called interrogation areas. This allows to infer the most likely particle displacement and to compute the motion vectors. It is also known from [4] as the cross correlation method. In this work, we use the Matlab implementation available in the PIVlab library [16]. Unlike the existing literature, we apply PIV on binary rather than on gray-scale images. The number of interrogation areas in an image, thus the number of vectors, is a parameter of the algorithm. In this case, it is chosen trough a sensitivity analysis as the one which leads to the best performance, as shown in Section IV. The cloud motion vectors of the image are averaged in order to obtain a global motion vector.

3) Persistent method: This method assumes that the clouds are persistent in a short-term horizon, and therefore the global cloud motion vector is zero.

E. Cloud map forecasting

It consists in translating the current cloud map according to the global motion vector, which is scaled in magnitude according to the forecasting horizon to achieve. This leads to the so-called forecasted cloud map. It was observed empirically that averaging the last 5 motion vectors rather than using the last one only leads to better forecasted cloud maps.

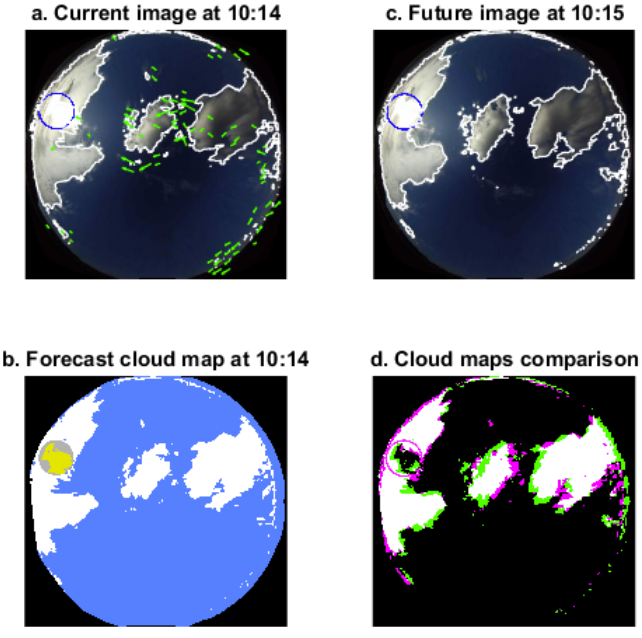

Fig. 2. Example of the forecasted cloud map procedure.

An example of the procedure described until this stage is shown in Fig. 2. Fig. 2a shows the undistorted view of the sky with the sun location (blue circle) and PIV motion vectors (green arrows). The global motion vector, obtained by

averaging the PIV vectors, is used to translate the cloud map obtained by segmenting Fig. 2a. The translated cloud map is shown in Fig. 2b, where the white color denotes cloudy pixels, blue clear sky, and yellow circumsolar region. Fig. 2c shows the 1 minute ahead realization. Fig. 2d compares the forecasted cloud map (purple color) against the future ground truth cloud map from Fig. 2c (green color). The white color denotes those pixels which are correctly classified as cloudy.

F. Local cloud cover computation

The forecasted local cloud cover is computed as the percentage of cloudy pixels in the forecasted cloud map in a region around the sun. The region we consider is a disk with 100 pixels radius (at this stage, this is chosen empirically). We consider a circumsolar area rather than the whole picture since this is the region with the largest interest when considering short-term sun occlusions by clouds.

G. GHI prediction intervals computation

The work in [2] describes a method to compute GHI prediction intervals (PIs) with look-ahead time in the range from seconds to minutes starting from historical GHI measurements. We augment this algorithm by including the local cloud cover as an additional influential variable. The PI, which is defined as the interval where the future realization is expected to fall with a designed confidence level α [17], is denoted in the following formulation as $\left(I^{\uparrow\alpha}_{t+1|t}, I^{\downarrow\alpha}_{t+1|t}\right)$. The original method in [2] consists in grouping N historical values of the differentiated GHI time series ΔI into k clusters according to the value of two selected data features:

- the average GHI value on a mobile window of length n, considering the most recent data points:

$$M_i = \frac{1}{n}\sum_{j=i-n}^{i} \Delta I_j, \qquad i = n+1, \ldots, N; \quad (3)$$

- the GHI variability, defined as:

$$V_i = \sqrt{\frac{1}{n}\sum_{j=i-n}^{i} \left(\Delta I_j - \Delta I_{j-1}\right)^2}, \quad i = n+1, \ldots, N. \quad (4)$$

The clustering process produces k clusters $G_1, \ldots, G_k$ and their centroids $\mathbf{c_1}, \ldots \mathbf{c_k}$; the histograms of the clusters are assumed as the empirical probability distribution function of the variations with respect to the one-step-ahead irradiance realization. During real-time operation, the data features vector at time t, denoted by $\mathbf{p_t} = (M_t, V_t)$, is calculated. The next step is the calculation of the Euclidean distances between $\mathbf{p_t}$ and the centroids $\mathbf{c_l}$

$$d_l = \|\mathbf{c_l} - \mathbf{p_t}\|^2, \;\; l = 1, ..., k \quad (5)$$

which is used as a similarity criterion to select the cluster representative of the future irradiance value. With respect to the original method, we add the local cloud cover (obtained from the procedure described above) as an additional feature to build the clusters.

Finally, we compare three different combinations of influential variables:

- average irradiance and its variability (henceforth called *GHI measurements* in Section IV-G);
- average irradiance, its variability and the local cloud cover (henceforth called *Images + GHI measurements*);
- local cloud cover only (henceforth called *Images*).

IV. Results

A. Experimental setup

GHI observations are from an Apogee SP-230 all-season pyranometer installed near the camera. Pyranometer GHI measurements are with an error of 2% and 5% at solar zenith angles of 45 and 75 degrees, respectively. ASIs and GHI measurements are synchronized and stored in a database.

B. Image metrics

To evaluate the performance of cloud detection and cloud motion identification, we define the matching error similarly to [4]. Let C be the ground truth cloud map (e.g., from manual segmentation), $\widehat{C}$ the estimated cloud map, and N the total number of pixels in the image. The matching error is:

$$matching\ error = \frac{1}{N}\sum_{i=1}^{I}\sum_{j=1}^{J}\left|C_{ij} - \widehat{C}_{ij}\right| \quad (6)$$

The matching error is used in the work, i), to assign the parameters of the Schmidt's algorithm (as described earlier), ii), cloud detection performance assessment, and, iii), evaluation of the cloud motion algorithms.

C. Forecasting performance metrics

To determine the quality of the prediction intervals of the probabilistic forecasting algorithm, we use the Prediction Interval Coverage Probability (PICP) and the Prediction Interval Normalized Averaged Width (PINAW), [18]. The PICP counts the number of times that the realization falls inside the PI for a given confidence level α:

$$\text{PICP} = \frac{1}{L}\sum_{t=1}^{L} c_t \quad (7)$$

where L is the total number of forecast instances of the testing dataset and

$$c_t = \begin{cases} 1, & \hat{I}^{\downarrow\alpha}_{t+1|t} \le I_{t+1} \le \hat{I}^{\uparrow\alpha}_{t+1|t} \\ 0, & \text{otherwise.} \end{cases} \quad (8)$$

where I_{t+1} is the one-step ahead GHI realization. The PINAW measures the width of the prediction interval:

$$\text{PINAW} = \frac{1}{LI_{max}}\sum_{t=1}^{L}(\hat{I}^{\uparrow\alpha}_{t+1|t} - \hat{I}^{\downarrow\alpha}_{t+1|t}), \quad (9)$$

where $I_{max} = 1000\ \text{W/m}^2$.

D. Cloud detection performance assessment

Cloud detection is the first step of the prediction tool-chain. Its accuracy plays a crucial role and it is therefore relevant to quantify it. The average matching error Eq. 6 calculated over the set of the 40 manually segmented pictures is 18%.

E. Selection of the number of motion vectors for PIV

We implement a sensitivity analysis to determine the best number of motion vectors for PIV. In general, the number of vectors depends on the size (in number of pixels) of the first and second interrogation areas. We have tested different combinations for the size of the interrogation areas, as reported in Table II. This allowed to determine the combination leading to the smallest matching error into the forecasted cloud map. The best combinations of interrogation areas are 400×400 and 200×200 pixels for interrogation areas 1 and 2, respectively, for the 1 and 2 minutes forecast horizons, while they are 200×200 and 100×100 pixels for interrogation areas 1 and 2, respectively, for the 5 and 10 minutes forecast horizons. These combinations the sizes used in the following for the PIV interrogation areas.

TABLE II
TESTED PIV VECTORS AND INTERROGATION AREAS

Number of vectors	42×45	29×31	27×29	25×27	20×22
Interrogation area 1	200	280	300	320	400
Interrogation area 2	100	140	150	160	200

F. Performance assessment of cloud motion methods

In this section, the performance of the three considered cloud motion methods (HMD, PIV and persistence) is compared in terms of the matching error of their forecasted cloud maps. Here, the testing image dataset consists in 40 consecutive images captured during partly-cloudy conditions. Results are shown in Fig. 3 and summarized in Table III. We obtain that:

- at 1 minute look-ahead time, the HMD method is the best performing;
- at 2 minutes, the HMD and the PIV have a similar performance and outperform the persistence method;
- at 5 and 10 minutes, neither the HMD nor the PIV outperforms the benchmark persistence model.

The last result is likely due to the fact that the considered cloud motion algorithms do not model phenomena such as cloud generation, dissipation and cloud shape changing, all effects which become more prominent when considering longer forecasting horizon.

G. GHI forecast assessment

To compute the forecasted local cloud cover and test its influence on the GHI forecasting tool, we choose the best performing cloud motion algorithm according to the look-ahead time. From the previous section, these are: HMD at 1 minute, PIV at 2 minutes, and persistence model at 5 and 10 minutes forecast horizon.

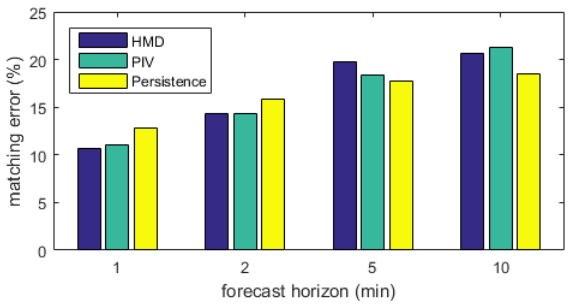

Fig. 3. Cloud motion methods evaluation for different forecast horizons.

TABLE III
MATCHING ERROR (%)

Forecast horizon	1 min	2 min	5 min	10 min
HMD	10.65	14.34	19.72	20.68
PIV	11.08	14.27	18.42	21.23
Persistence	12.83	15.82	17.68	18.44

Table IV shows the Pearson correlation coefficients between the time series of GHI and local cloud cover (considering measurements spanning a 21 days long period) on four distinct forecast horizons (1, 2, 5 and 10 minutes). A high correlation is observed between the two variables, thus suggesting that the local cloud cover is a meaningful variable that can be used to improve the accuracy of GHI forecast methods.

TABLE IV
PEARSON CORRELATION COEFFICIENTS

Forecast horizon	**1 min**	**2 min**	**5 min**	**10 min**
Cloud motion method	HMD	PIV	Persistence	
Correlation coefficient	-0.7622	-0.7985	-0.7806	-0.7504

We consider the probabilistic forecasting tool described in Section III-G. The training and testing data set consists of measurements for 16 and 5 days, respectively. We select a number of clusters k manually tuned to achieve a coverage probability very close to the target confidence level $\alpha = 95\%$.

Results are summarized in tables V and VI, and shown in Fig. 4. They can be summarized as follows:

- from Table V, all the considered cases have a coverage probability (PICP) close to the target confidence level (95%), denoting that the methods have a good reliability;
- in any case, adding the forecasted local cloud cover to GHI measurements is beneficial as it improves the GHI forecast on all the considered forecasting horizons (or it does not impact negatively, as in the 1 minute case);
- the use of the forecasted local cloud cover as only influential variable outperforms all the other methods at 1, 2, and 5 minutes forecast horizons.

V. CONCLUSION AND FUTURE WORKS

We have carried a first investigation on how to augment a GHI time series-based forecasting tool for solar irradiance

TABLE V
PICP (%)

Forecast horizon	1 min	2 min	5 min	10 min
GHI measurements	96.06	95.6	95.14	97.2
Images + GHI measurements	94.75	95.16	96.45	97.23
Images	94.92	94.56	94.75	95.95

TABLE VI
PINAW (%)

Forecast horizon	1 min	2 min	5 min	10 min
GHI measurements	4.13	7.05	12.69	18.12
Images + GHI measurements	4.13	6.89	12.23	16.69
Images	3.6	5.78	11.87	17.39

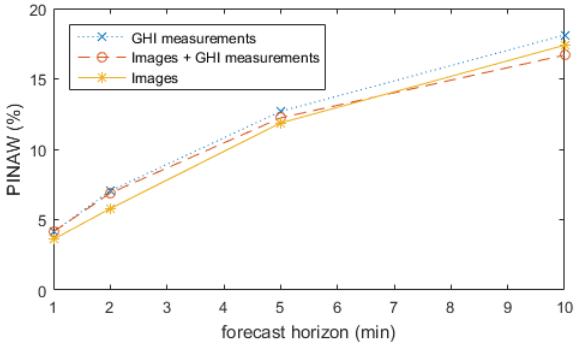

Fig. 4. PINAW of the GHI prediction for different forecast horizons.

by using information on the cloud motion extracted from all-sky images. The cloud motion algorithms considered in the analysis are particle image velocimetry (PIV, from the literature), heuristic motion detection (HMD, an original method described in this work), and a persistent predictor.

It was shown that applying cloud motion identification allows to improve cloud map forecasting performance up to the 2 minutes forecasting horizon. Above the 2 minutes look-ahead time, there is no advantage with respect to using a persistance predictor.

Results on GHI prediction intervals shows that including information on the cloud motion is in general beneficial because it leads to get smaller PIs width.

The future work is in the direction of consolidating the current results by extending the proposed method to an alternative all-sky imager, and comparing the results with those obtained from cloud detection methods based on machine learning strategies.

REFERENCES

[1] R. Palma-Behnke, C. Benavides, F. Lanas, B. Severino, L. Reyes, J. Llanos, and D. Sáez, "A microgrid energy management system based on the rolling horizon strategy," *IEEE Transactions on Smart Grid*, vol. 4, no. 2, pp. 996–1006, 2013.

[2] E. Scolari, F. Sossan, and M. Paolone, "Irradiance prediction intervals for pv stochastic generation in microgrid applications," *Solar Energy*, vol. 139, pp. 116–129, 2016.

[3] T. Schmidt, J. Kalisch, E. Lorenz, and D. Heinemann, "Evaluating the spatio-temporal performance of sky-imager-based solar irradiance analysis and forecasts," *Atmospheric chemistry and physics*, vol. 16, pp. 3399–3412, March 2016.

[4] C. W. Chow, B. Urquhart, M. Lave, A. Dominguez, J. Kleissl, J. Shields, and B. Washom, "Intra-hour forecasting with a total sky imager at the uc san diego solar energy testbed," *Solar Energy*, vol. 85, no. 11, pp. 2881–2893, 2011.

[5] R. Marquez and C. Coimbra, "Intra-hour dni forecasting based on cloud tracking image analysis," *Solar Energy*, vol. 91, no. 99, pp. 327–336, April 2013.

[6] Y. Chen, W. Li, C. Zhang, and C. Hu, "Global velocity constrained cloud motion prediction for short-term solar forecasting," *Application of digital image processing*, vol. 9971, 2016.

[7] S. Sun, E. Ritzhaupt-Kleiss, and T. Chen, "short term cloud coverage prediction using ground based all sky imager," *IEEE international conference on smart grid communications*, vol. 14, 2014.

[8] S. Quesada-Ruiz, Y. Chu, J. Tovar-Pescador, H. Pedro, and C. Coimbra, "Cloud-tracking methodology for intra-hour dni forecasting," *Solar Energy*, vol. 102, pp. 267–275, 2014.

[9] D. Bernecker, C. Riess, A. Elli, and J. Hornegger, "Continuous short-term irradiance forecasts using sky images," *Solar Energy*, vol. 110, pp. 303–315, September 2014.

[10] Y. Chu, M. Li, H. T. Pedro, and C. F. Coimbra, "Real-time prediction intervals for intra-hour dni forecasts," *Renewable Energy*, vol. 83, pp. 234–244, 2015.

[11] H. T. Pedro and C. F. Coimbra, "Nearest-neighbor methodology for prediction of intra-hour global horizontal and direct normal irradiances," *Renewable Energy*, vol. 80, pp. 770–782, 2015.

[12] H.-Y. Cheng, C.-C. Yu, and S.-J. Lin, "Bi-model short-term solar irradiance prediction using support vector regressors," *Energy*, vol. 70, pp. 121–127, 2014.

[13] R. W. Andrews, J. S. Stein, C. Hansen, and D. Riley, "Introduction to the open source pv lib for python photovoltaic system modelling package," in *Photovoltaic Specialist Conference (PVSC), 2014 IEEE 40th*. IEEE, 2014, pp. 0170–0174.

[14] M. R. Calabretta and E. W. Greisen, "Representations of celestial coordinates in fits," *Astronomy & Astrophysics*, vol. 395, no. 3, pp. 1077–1122, 2002.

[15] Z. Zhang, "A flexible new technique for camera calibration," *IEEE Transactions on pattern analysis and machine intelligence*, vol. 22, no. 11, pp. 1330–1334, 2000.

[16] W. Thielicke and E. J. Stamhuis, "Pivlab-toward user-friendly affordable and accurate digital particle image velocimetry in matlab," *Journal of open research software*, vol. 28, no. 99, pp. 1286–1296, April 2014.

[17] P. Pinson, "Estimation of the uncertainty in wind power forecasting," Ph.D. dissertation, École Nationale Supérieure des Mines de Paris, 2006.

[18] A. Khosravi, S. Nahavandi, and D. Creighton, "Prediction intervals for short-term wind farm power generation forecasts," *Sustainable Energy, IEEE Transactions on*, vol. 4, no. 3, pp. 602–610, 2013.